Journal of Innovative Optical Health Sciences
Vol. 3, No. 2 (2010) 109–121

DOI: 10.1142/S1793545810000976

COMPARISON OF OPTICAL POLARIMETRY AND DIFFUSION TENSOR MR IMAGING FOR ASSESSING MYOCARDIAL ANISOTROPY

MARIKA A. WALLENBURG*, MIHAELA POP†, MICHAEL F. G. WOOD*, NIRMALYA GHOSH‡, GRAHAM A. WRIGHT† and I. ALEX VITKIN§,¶

*Ontario Cancer Institute, Division of Biophysics and Bioimaging
University Health Network and University of Toronto
Department of Medical Biophysics, 610 University Avenue
Toronto, Ontario, Canada M5G 2M9

†Department of Medical Biophysics, University of Toronto
Sunnybrook Health Sciences Center, 2075 Bayview Avenue
Toronto, ON, Canada, M5N 3M5

‡IISER Kolkata, Mohanpur Campus, P. O. BCKV Campus Main Office
Mohanpur 741252, West Bengal, India

§Ontario Cancer Institute, Division of Biophysics and Bioimaging
University Health Network and University of Toronto
Departments of Medical Biophysics and Radiation Oncology
610 University Avenue, Toronto, Ontario, Canada M5G 2M9
¶vitkin@uhnres.utoronto.ca

We have recently proposed an optical method for assessing heart structure that uses polarized light measurement of birefringence as an indicator of tissue anisotropy. The highly aligned nature of healthy cardiac muscle tissue has a detectable effect on the polarization of light, resulting in a measurable phase shift ("retardance"). When this organized tissue structure is perturbed, for example after cardiac infarction (heart attack), scar tissue containing disorganized collagen is formed, causing a decrease in the measured retardance values. However, these are dependent not only on tissue anisotropy, but also on the angle between the tissue's optical anisotropy direction and the beam interrogating the sample. To remove this experimental ambiguity, we present a method that interrogates the sample at two different incident beam angles, thus yielding enough information to uniquely determine the true magnitude and orientation of the tissue optical anisotropy. We use an infarcted porcine heart model to compare these polarimetry-derived anisotropy metrics with those obtained with diffusion tensor magnetic resonance imaging (DT-MRI). The latter yields the anisotropy and the direction of tissue water diffusivity, providing an independent measure of tissue anisotropy. The optical and MR results are thus directly compared in a common *ex vivo* biological model of interest, yielding reasonable agreement but also highlighting some technique-specific differences.

Keywords: Birefringence; Mueller matrix decomposition; fractional anisotropy; diffusion tensor magnetic resonance imaging; myocardial infarction.

1. Introduction

Cardiovascular disease is a major cause of death in the western world. Myocardial infarction (heart attack) in particular is associated with decreased contractile function, impaired ventricular function, and high mortality. During the healing process, the necrosis of cardiomyocytes is followed by scar formation and tissue remodeling, as the double-spiral structure of the heart is perturbed and patches of non-contractile collagenous scar tissue replace the muscle in areas deprived of adequate blood supply.[1] Both these effects reduce the heart's functionality by interfering with its normal contractile function.[2,3] Thus, knowledge of tissue composition and microstructural organization is important for assessing severity of injury.

Recently, we proposed a novel optical method of assessing myocardium structure after infarct, and after subsequent therapies based on stem-cell–induced regeneration, using polarized light measurement of linear retardance in birefringent tissue.[4] Historically, polarized light methodologies have not seen extensive use in biomedicine because of severe depolarizing effects caused by multiple scattering; nevertheless, some research on polarimetric tissue characterization has recently been reported, for instance in thermally damaged tissues,[5,6] using various polarized light parameters (including birefringence,[7,8] Stokes vectors,[9,10] and different rotationally invariant mathematical descriptions[11]). In the context of this work, anisotropic materials exhibit different indices of refraction in different directions, resulting in different light propagation speeds; optical anisotropy also manifests itself as an accumulating phase shift (retardance) between different polarization components of light traversing the birefringent material. Thus, highly aligned tissues (such as muscle fibers), will exhibit high retardance, while more isotropic tissues (such as collagenous scar), will show a lower retardance, providing a way of assessing the small-scale structure and microarchitectural organization of tissue.

Our initial polarimetry studies in cardiac tissues[4,12] relied on sensitive measurements of tissue polarization parameters and post-processing based on Mueller matrix decomposition to separate out and quantify the effects of tissue birefringence. With this methodology, linear retardance measurements assessed structural damage and regeneration in infarcted and stem-cell treated rat hearts.[12] Linear retardance, δ, was used as a measure of birefringence, $\Delta n = n_e - n_o$ (n_e and n_o are the refractive indices along the extraordinary and ordinary axes respectively), as the two are proportional:

$$\delta = \frac{2\pi}{\lambda} d\Delta n, \tag{1}$$

where d is the pathlength of photons and λ is the wavelength of light. It was found that linear retardance decreased following injury, with stem-cell treated hearts showing a less important decrease in retardance than untreated hearts.[12]

This effect is not straightforward to interpret, however, as the derived retardance values are dependent on the angle between the tissue's optical axis (orientation of the extraordinary axis) and the beam interrogating the sample,[13] a decrease in retardance value could be caused by a true decrease in tissue anisotropy, or by an experimental artifact due to interrogation beam — optical axis effects. Because of this angular dependence, the apparent birefringence,

$$\Delta n_{\text{app}} = n - n_o, \tag{2}$$

where n is the apparent index of refraction, depends on the direction of propagation of light with respect to the ordinary and extraordinary axes according to the following equation:

$$\frac{1}{n^2} = \frac{\sin^2 \gamma_c}{n_e^2} + \frac{\cos^2 \gamma_c}{n_o^2}, \tag{3}$$

where γ_c is the angle between the beam path and the extraordinary axis.[14] Thus, the apparent value of linear retardance δ_{app} will be maximal (and reflect "true" sample birefringence) when the light is propagated perpendicular to the extraordinary axis, and will be null when the light propagates along the extraordinary axis (see Fig. 1, where $\gamma_c = 90° - \psi$).

In this manuscript, we thus propose a dual projection polarimetry method whereby a sample is imaged twice with different orientations of the probing beam, yielding sufficient information to reconstruct the true magnitude and orientation of the tissue anisotropy. The azimuthal angle θ (i.e., the projection of the optical axis in the plane perpendicular to the interrogating light beam, see Fig. 1) can be determined by the Mueller matrix decomposition algorithm described previously.[4,15] By recording the apparent linear retardance δ_{app} and azimuthal angle θ measured with two different beam geometries, we can reconstruct the true magnitude and orientation of tissue anisotropy. This yields intrinsic metrics

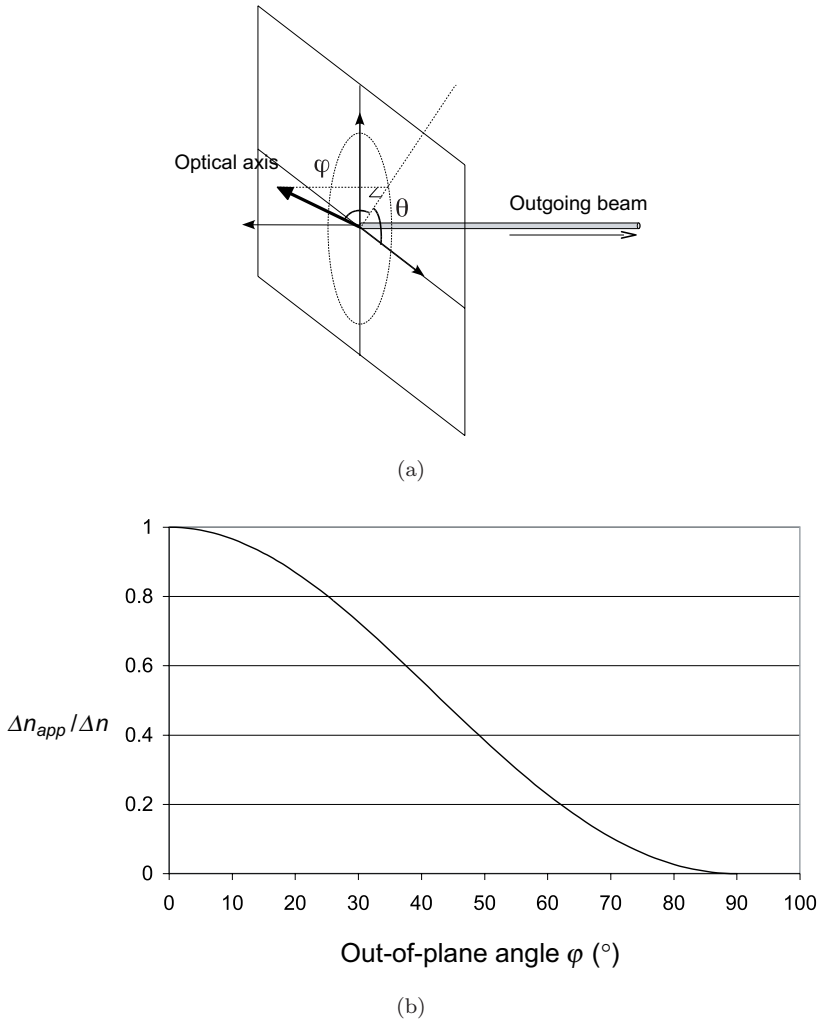

Fig. 1. Effect of tissue optical axis orientation. (a) Orientation of the tissue optical (anisotropy) axis: θ is the azimuthal angle, which can be determined from Mueller matrix decomposition; ψ is the out-of-plane angle. (b) Fraction of birefringence observed (apparent over real birefringence) as a function of the out-of-plane angle ψ. The apparent birefringence vanishes when the optical axis and probing beam are parallel ($\psi = 90°$).

of tissue micro-architecture, independent of experimental orientation effects. These metrics may be of particular interest in cardiology, as adverse remodeling of the heart following infarct causes loss of contractile function,[3] with partial recovery following regenerative treatments.[16]

To compare and validate the tissue anisotropy magnitude and orientation obtained with polarimetry, we use diffusion-tensor magnetic resonance imaging (DT-MRI), a well-established method used to derive fiber directions as well as parameters like fractional anisotropy, FA.[17] It has been shown that DT-MRI can yield information about tissue small-scale structure by revealing anisotropy in the diffusivity of water in a tissue. This technique has been validated against histology.[18] Analogous to the discussion above, in the case of myocardial infarction, the site of injury (i.e., the scar) is characterized by a decrease in diffusion anisotropy, as the collagenous scar tissue replaces the highly fibrillar structure of cardiac muscle.[19,20] Furthermore, the first eigenvector of the diffusion tensor (corresponding to the direction of the highest diffusion coefficient) is parallel to the direction of the fibers, thus directly revealing the axis of alignment of the muscle fibers. Thus, magnitude and direction of tissue anisotropy furnished by two independent methods, obtained from the same biological model of interest, can be directly compared. To further aid the comparison and data interpretation, we also provide corresponding histopathology (the gold standard method to assess tissue damage

and scar extent) using the whole-mount technique developed by Clarke *et al.*,[21] with further collagen-specific staining.

Thus, polarimetry and DT-MRI both report on tissue anisotropy, the former via optical refractive index properties, and the latter by water diffusion effects. In this paper, we present a comparison of both methods in an infarcted porcine heart. We first describe the biological model used for this study, and provide the details of the diffusion tensor MR imaging process. This is followed by the description of the polarimetry setup, decomposition method, image processing, and dual projection reconstruction method. We then present and compare the anisotropy magnitude and direction results as obtained by DT-MRI and polarimetry. Finally, we discuss the agreements and disagreements observed with the two methods, limitations of this work, and future directions.

2. Methods and Materials

2.1. *Cardiac animal model and sample preparation*

In this study, a porcine chronic infarct model was used. All surgical procedures were performed in accordance with Sunnybrook Research Institute (Toronto, Canada) regulations, under an approved EUA protocol. The infarction was created by 90 minute balloon occlusion of the left circumflex artery, followed by reperfusion (flow restoration). The animal was allowed to heal for six weeks, which generated a chronic infarct characterized by collagen deposition and formation of fibrous scar tissue, as well as an alteration of fiber architecture and anisotropy, as demonstrated later by histological assessment. The heart was excised and fixed in formalin, after which DT-MRI was performed. Finally, sections were taken from an axial slice in infarcted and non-infarcted regions of the left ventricular wall, and were sectioned to 400 μm thick slices in preparation for polarimetry assessment. Confirmatory histopathology was also performed: the whole-mount samples were prepared as in Clarke *et al.*[21] and further were stained with Picrosirius Red.

2.2. *Diffusion tensor imaging and analysis*

The excised and fixed heart sample was imaged using a 1.5 Tesla Signa GE MR scanner (GE Healthcare, Milwaukee, WI). Prior to MR imaging studies, the whole heart was placed in a phantom box filled with Fluorinert, a fluorocarbon-based fluid which has negligible MR signal, for characterization of the fibers' fractional anisotropy. The diffusion-weighted imaging sequence is based on a 3D fast spin echo (FSE) sequence with diffusion gradients applied in seven directions, that allows calculation of diffusion tensor.[22] The following MR parameters were used: TE = 20–30 ms, TR = 700 ms, NEX = 1, b-value = 600, seven directions for diffusion gradients, with slice thickness = 1.5 mm, a FOV and matrix yielding an in-plane interpolated resolution of approximately 0.5 × 0.5 mm. Imaging time was approximately 10 hours.

Fractional anisotropy (FA), a measure that describes the degree of anisotropy in the diffusion of water molecules along the myocardial fibers, is given by the following equation:

$$\mathrm{FA} = \sqrt{\frac{3}{2}}\frac{\sqrt{(\lambda_1-\lambda)^2+(\lambda_2-\lambda)^2+(\lambda_3-\lambda)^2}}{\sqrt{\lambda_1^2+\lambda_2^2+\lambda_3^2}}, \tag{4}$$

where $\lambda_{1,2,3}$ are the eigenvalues of the diffusion tensor, and λ is the mean diffusivity.[23] The FA has values between 0 (isotropic diffusion) and 1 (infinite anisotropy). At each voxel, the FA will give the relative degree of anisotropy, dominated by the largest component (largest eigenvalue of the diffusion tensor). In the case of a cylindrically symmetric anisotropic medium, such as myocardial fibers, $\lambda_1 \gg \lambda_2 = \lambda_3$ and FA ≈ 1. The anisotropy maps (color-coded and/or black and white) were visualized in short axis MRI views with MedINRIA[24] and DTI-Studio[25] software.

2.3. *Polarimetry imaging and analysis*

2.3.1. *Experimental polarimetry system*

The experimental polarimetry system measures the polarization of the light after it has interacted with the sample. By finding the output polarization state for different input polarization states, the sample's polarization transfer function can be determined, in the form of a four-by-four Mueller matrix which contains information about the polarization properties of the sample. The polarization of a beam of light is represented with a four-element Stokes vector $\mathbf{S} = (I\,Q\,U\,V)^T$. The element I represents the overall intensity of the beam, Q gives the intensity of linear polarization along horizontal and vertical

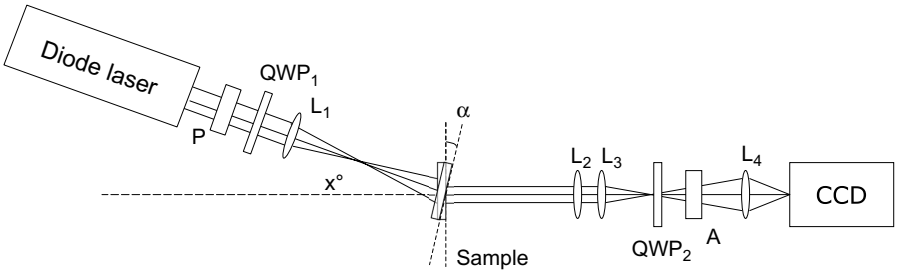

Fig. 2. Schematic of the polarimetry imaging system. P: polarizer; L_i: lenses; QWP_i: quarter-wave plate; A: analyzer. The input beam is off-axis by x° in order to avoid direct light saturating the CCD.

axes, U gives the intensity of linear polarization at $\pm 45^\circ$, and V gives the intensity of light that is (right- and left-) circularly polarized. The Mueller matrix describes the effect of any optical element on the polarization of light: for a given initial polarization state $\mathbf{S_i}$, the polarization of light after interaction with the optical element with Mueller matrix $\mathbf{M}$ will be $\mathbf{S_o} = \mathbf{M}\mathbf{S_i}$. The complexities inherent in Mueller matrix polarimetry, including the issues associated with unique parameter extraction from its 16 elements, are discussed in greater detail below.

Figure 2 shows a schematic of the polarimetry imaging system used for this experiment. Light from a 635-nm diode laser (ThorLabs) is used, as tissue absorption is low at this wavelength. The polarization state of the incident light is controlled using a removable quarter-wave plate and a linear polarizer. The incident light beam is angled off axis ($\approx 20^\circ$) in order to avoid directly transmitted light saturating the CCD (Photometrics CoolSnap K4). As the beam exits the sample, a removable quarter-wave plate and linear analyzer select a single polarization state of the outgoing light, which is finally detected with a CCD camera. While systems with dynamic polarization modulation and synchronous detection have been used previously to increase signal-to-noise ratio[15] (by using a photoelastic modulator to modulate the light polarization at a known frequency), a simpler setup was deemed sufficient for this study. Four input states (horizontal, vertical, $+45^\circ$, right-circularly polarized) and six output states (horizontal, vertical, $\pm 45^\circ$, right- and left-circularly polarized light) were recorded for a total of 24 combinations per sample. The output Stokes parameters for each input state were measured from the detected intensities as

$$\begin{aligned} I &= I_{180^\circ} + I_{90^\circ}, \\ Q &= I_{180^\circ} - I_{90^\circ}, \\ U &= I_{45^\circ} - I_{135^\circ}, \\ V &= I_R - I_L, \end{aligned} \tag{5}$$

where the subscripts indicate the output state being detected (as determined by the presence or absence of the quarter-wave plate, and the orientation of the analyzer). Finally, the 16 elements of the Mueller matrix were calculated as follows:

$$\mathbf{M}(i,j) = \begin{bmatrix} \frac{1}{2}(I_H + I_V) & \frac{1}{2}(I_H - I_V) & I_P - \mathbf{M}(1,1) & I_R - \mathbf{M}(1,1) \\ \frac{1}{2}(Q_H + Q_V) & \frac{1}{2}(Q_H - Q_V) & Q_P - \mathbf{M}(2,1) & Q_R - \mathbf{M}(2,1) \\ \frac{1}{2}(U_H + U_V) & \frac{1}{2}(U_H - U_V) & U_P - \mathbf{M}(3,1) & U_R - \mathbf{M}(3,1) \\ \frac{1}{2}(V_H + V_V) & \frac{1}{2}(V_H - V_V) & V_P - \mathbf{M}(4,1) & V_R - \mathbf{M}(4,1) \end{bmatrix}, \tag{6}$$

where the indices i and j denote the rows and columns respectively, and where the subscript corresponds to the input polarization state (as determined by the presence or absence of the quarter-wave plate, and the orientation of the polarizer).

This experimentally-determined Mueller matrix reflects the lumped description of simultaneously occurring complex processes such as depolarization, diattenuation, and retardance.[26,27] As such, its 16 elements reflect a complex interplay of

these processes, and unique interpretation of the results, including extraction and quantification of a particular process of interest, is highly problematic. In order to extract individual polarization effects, Mueller matrix decomposition was performed (more details in Sec. 2.3.2) to extract the sample's polarizing properties, including retardance. This process is repeated at each pixel (pixel size $\approx 40\,\mu\text{m} \times 40\,\mu\text{m}$).

In order to perform dual projection reconstruction, imaging was done twice for each sample: with the sample plane perpendicular to the outgoing beam, and with the sample plane rotated slightly by angle α (see Fig. 2). This angle must be small enough that (i) the photon pathlength through the sample is not changed significantly between the two projections, and (ii) the images recorded by the CCD are similar enough to be registered to one another, despite the slightly different camera perspectives.

2.3.2. *Mueller matrix decomposition*

A detailed description of the Mueller matrix decomposition that was used has been published elsewhere,[4,15] so only a brief overview of the relevant sections will be provided here. In turbid, optically active media, depolarization, linear and circular birefringence, and linear and circular dichroism can all be present and occur simultaneously, making interpretation of the Mueller matrix (which represents the lumped effect of all these interactions) non-trivial. It has been shown that, using a process known as Mueller matrix decomposition, the full Mueller matrix $\mathbf{M}$ can be decomposed into the product of three constituent matrices reflecting the three optical interactions, as follows:

$$\mathbf{M} = \mathbf{M_\Delta M_R M_D}, \tag{7}$$

where the effects of depolarization are described by the depolarizing matrix $\mathbf{M_\Delta}$, the effects of linear birefringence and optical activity (circular birefringence) are described by the retarder matrix $\mathbf{M_R}$, and the effects of linear and circular dichroism are described in the diattenuator matrix $\mathbf{M_D}$.[4,28] While matrix multiplication is non-commutative [and thus the order in Eq. (7) is not unique], it has been shown that for weakly diattenuating turbid media such as most biological tissues, the extracted polarization parameters are approximately independent of the multiplication order of the constituent matrices.[29] The validity and accuracy of this approach in turbid media have been previously demonstrated with both polarization-sensitive Monte Carlo simulations and with experimental data.[4,29]

The measurable effect of birefringence, the (apparent) linear retardance value δ (or δ_{app}), is contained in the retarder matrix $\mathbf{M_R}$ and can be calculated from its elements as[27]

$$\delta = \cos^{-1}\left(\sqrt{\begin{array}{c}(m_R(2,2)+m_R(3,3))^2 \\ +(m_R(3,2)-m_R(2,3))^2\end{array}} - 1\right), \tag{8}$$

where $m_R(i,j)$ are the elements of $\mathbf{M_R}$. Obtaining the value of θ, the orientation of the projection of the optical axis in the plane perpendicular to the probing beam (see Fig. 1), requires that the matrix $\mathbf{M_R}$ be further decomposed into $\mathbf{M_R} = \mathbf{M_{LR}M}_\phi$, in order to separate the effects of the linear retardance (contained in the matrix $\mathbf{M_{LR}}$) from those of chirality (contained in the matrix $\mathbf{M}_\phi$). The orientation θ can be calculated from the elements of $\mathbf{M_{LR}}$ as

$$\theta = 0.5\tan^{-1}\left(\frac{m_{LR}(2,3)-m_{LR}(3,2)}{m_{LR}(3,1)-m_{LR}(1,3)}\right). \tag{9}$$

If the light propagation distance d is known, the measured retardance δ can be used to calculate the sample birefringence [via Eq. (3)]. However this is not precisely known due to tissue scattering effects (although polarization-sensitive Monte Carlo simulations can be used to estimate the effective pathlength[30,31]), so in the current study we restrict ourselves to comparing retardance measurements in samples of uniform thickness ($400\,\mu\text{m}$).

2.3.3. *Image processing*

Since the field of view of the polarimetry imaging system ($\approx 1\,\text{cm} \times 1\,\text{cm}$) is smaller than the sample size ($\approx 3\,\text{cm} \times 2\,\text{cm}$), images of multiple regions were merged to form a single image for each projection. The two different projections for each sample were then registered with one another by aligning the edges of the sample in each image, so that the two projections could be compared pixel-by-pixel.

Because retardance arises from a phase shift between two orthogonal polarization states, a phase wrap-around artifact appears when the phase shift reaches and exceeds a value of 180°, introducing an ambiguity in the measurements. Thus, the maximal value that we can measure unambiguously is 180°: as the phase shifts reaches and exceeds 180°, the measured linear retardance value will peak and then

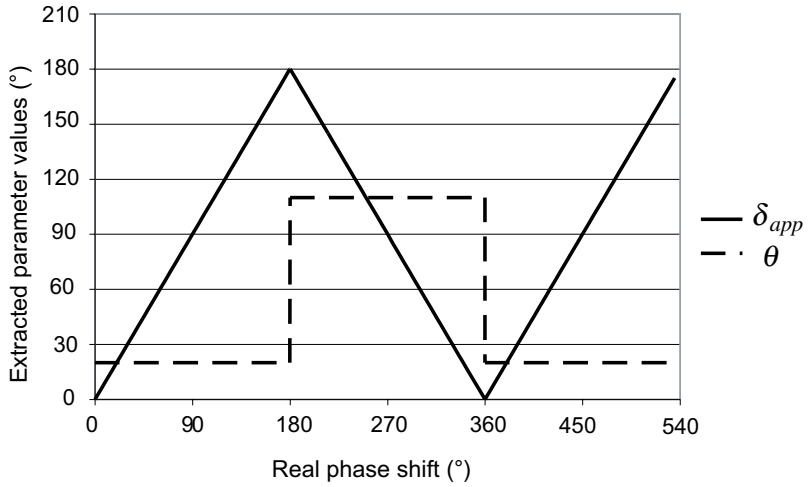

Fig. 3. Effect of wrap-around artifact on two extracted parameters: wrapped-around linear retardance δ (solid line) and orientation θ (dashed line) (as obtained from Mueller matrix decomposition), as a function of increasing real phase shift, for a material with (real) orientation $\theta = 20°$.

decrease until no linear retardance is measured at all (when the real phase shift is of 360°), so that for example, a phase shift of 188° will result in a measured linear retardance value of 172° (see Fig. 3). While measured linear retardance values are a continuous function of phase shift, values of orientation are discontinuous at each multiple of 180°: each multiple of 180° introduces a sign error that changes the value of the orientation by 90°.

The spatial imaging information allows this discontinuous orientation effect to be exploited in order to significantly reduce the ambiguity due to phase wrap-around. Changes in orientation of 90° over a distance of a single pixel are highly unphysical, and therefore can be used as a marker of phase wrap-around artifact, by creating a dividing line of pixels between two regions when a linear retardance multiple of 180° is reached. From the expectation that linear retardance should drop at the very edges of the sample (where certain photons have decreased pathlength, resulting in lower retardance values), it can be determined which side of this dividing line of pixels is wrapped-around. This extends the range of unambiguous measurements of linear retardance to 360°.

2.3.4. *Dual projection reconstruction*

As seen in Eq. (3), the apparent linear retardance is not only a function of the birefringence, but will vary experimentally depending on the angle between the probing beam and the optical axis of the material. In order to negate this experimental effect and derive true tissue anisotropy (its magnitude and direction), the optical axis of the material was determined and was then used to find an orientation-independent measure of anisotropy. For the purpose of this study, we will call this measure of the "maximum linear retardance", δ', as it corresponds to the value of linear retardance which *would be measured* through a slice of equal thickness and birefringence *if the optical axis were perpendicular to the probing light beam*; that is, the value of $\delta_{\text{app}} = \delta$ in the case where $\Delta n_{\text{app}} = \Delta n$ [see Eq. (3)]. As the samples presented here are all of a uniform thickness, the maximum linear retardance δ' can be compared between samples, and is directly proportional to the (true, not apparent) birefringence.

To achieve this, the sample was imaged twice with different orientations of the sample with respect to the probing beam: with the sample perpendicular to the beam ($\alpha = 0°$, see Fig. 2) and with the sample rotated by $\alpha = 12°$. The known behavior of the apparent refractive index [from Eq. (3)] was used to find the single optical axis consistent with both sets of measurements, yielding the magnitude and direction of tissue anisotropy. Finally, the images and coordinate system were rotated to correspond to the coordinate system of the DT-MRI images to facilitate optical — MR comparison.

3. Results and Discussion

Figure 4 shows the two sections used for polarimetry imaging, the corresponding axial section of the

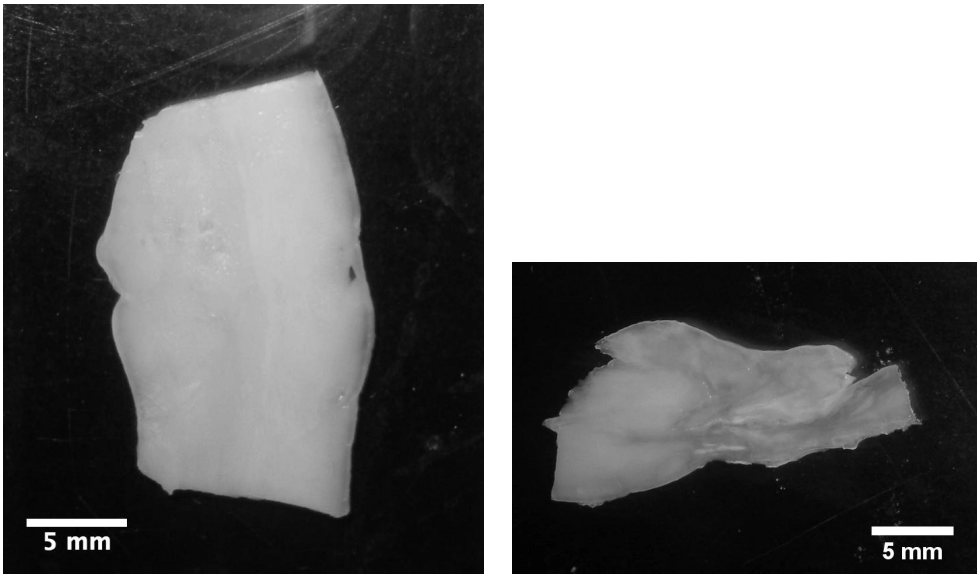

(a) (b)

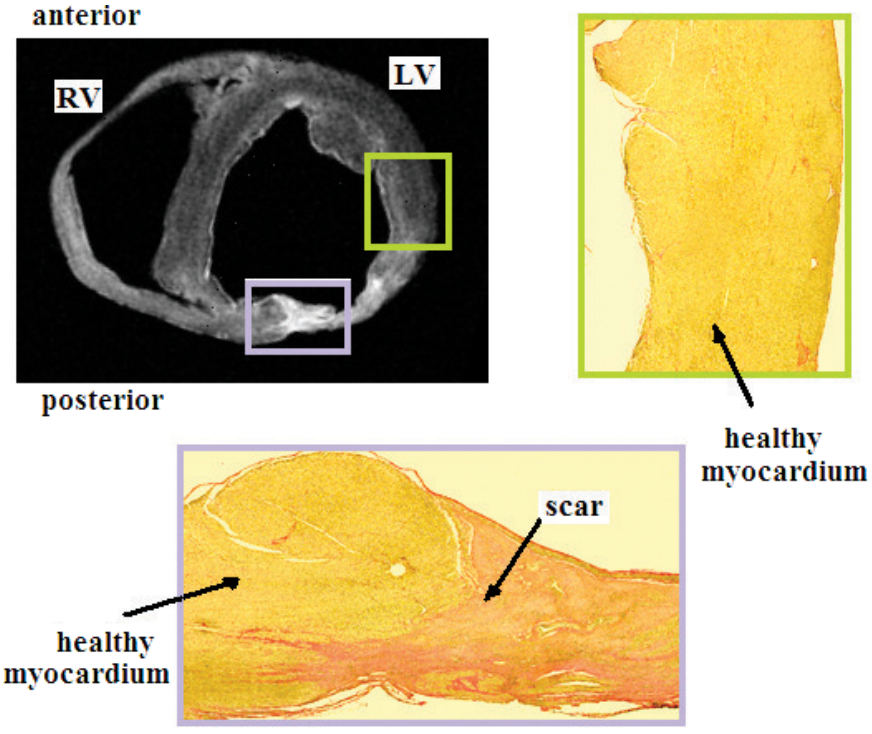

(c)

Fig. 4. (a) and (b): Healthy and infarcted regions of the left ventricular wall used for polarimetry imaging. (c) DT-MRI b0 image (unweighted image, i.e., with no applied diffusion gradient), with corresponding histology sections corresponding to healthy and infarcted regions, stained with Picrosirius Red.

DT-MRI data, and the corresponding histology sections. The first section (from the antero-lateral portion of the ventricle) is remote from the site of infarct; the second section (from the posterior portion of the ventricle, within the left circumflex artery territory) is located in the region of the infarct. The histology section shows very little collagen presence (stained red with Picrosirius Red) in the region corresponding to the healthy section, and a large quantity of collagen present in the area from the infarcted section, as expected from the formation of a collagenous scar.

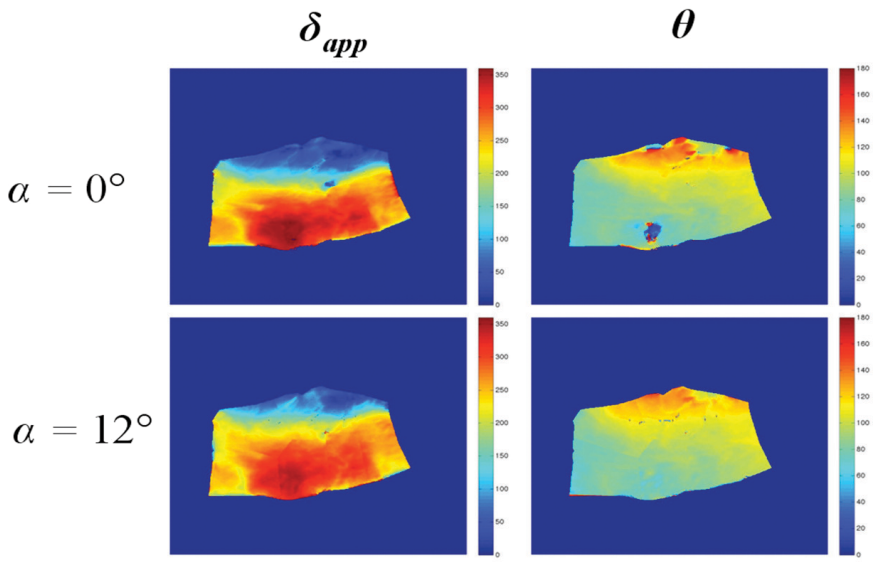

Fig. 5. Apparent linear retardance (δ_{app}, scale 0°–360°) and orientation (θ, scale 0°–180°), in degrees, as observed for the healthy sample in two different sample positions ($\alpha = 0$ and $\alpha = 12°$), after correction for phase wrap-around. The orientation is measured with respect to the vertical in this image, so that $\theta = 45°$ corresponds to an optical axis aligned along the top-left to bottom-right diagonal.

The values of apparent linear retardance δ_{app} and orientation θ for the healthy sample are shown in Fig. 5. Note that the highest values of apparent linear retardance approached 360°; if the photon pathlength is taken to be approximately the same as the thickness of the sample, this corresponds to a maximal birefringence value of 0.0016, which is roughly consistent with other published values of birefringence in pig heart.[32] From the two-projection sets of linear retardance and orientation values, a pixel-by-pixel reconstruction of the optical axis and maximal linear retardance δ' was performed, yielding a true magnitude and a 3D orientation of anisotropy for every pixel. Note that this method carries the implicit assumption that the tissue orientation is uniaxial and uniform over the thickness of the sample (400 μm).

Figures 6 and 7 show the axis of anisotropy and maximal linear retardance δ' for the healthy and infarct regions respectively. The anisotropy orientation results are presented in a color-coded display where all directions refer to the axis of the heart: red corresponds to the lateral component of the orientation; green corresponds to the

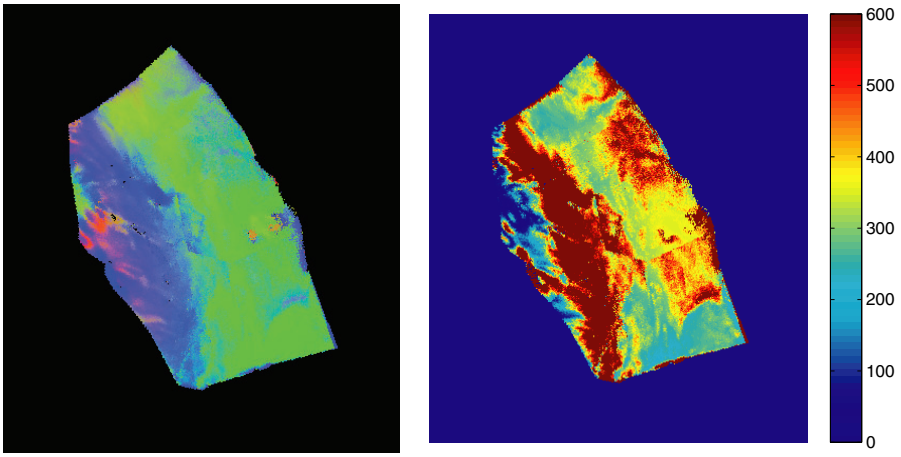

(a) (b)

Fig. 6. Polarimetry results of anisotropy axis and magnitude for the healthy region, as found with dual projection reconstruction. (a) Axis of anisotropy orientation. (b) Maximum linear retardance $\delta'(°)$ (scale 0°–600°).

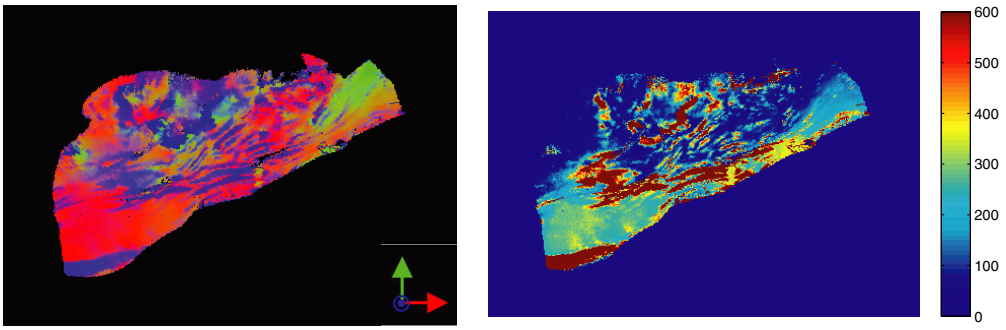

(a) (b)

Fig. 7. Polarimetry results of anisotropy axis and magnitude for the infarct region, as found with dual projection reconstruction. (a) Axis of anisotropy orientation. (b) Maximum linear retardance $\delta'(^\circ)$ (scale 0°–600°).

anterior-to-posterior component; and blue corresponds to the superior-to-inferior component. The axis of anisotropy in the healthy region is consistent with the expected double-spiral structure of the heart: the fibers are aligned circumferentially and horizontally (with respect to the heart's axis) in the middle of the ventricular wall, and progressively shift to a more vertical orientation towards the endocardium (and to a lesser extent also towards the epicardium). This is roughly consistent with normal (uninfarcted) myocardial structure.[2,33] The maximal linear retardance values mostly lie between 300° and 450°, with higher values (≥600°) in a thin region near the endocardium. (Note that while the *maximal* linear retardance values exceed 360°, the *apparent* linear retardance remain in the unambiguous value range of 0°–360°, so that the phase wrap-around artifact is accounted for.) In contrast to healthy cardiac tissue, the axis of anisotropy in the infarct region shows high variations in orientation, especially toward the endocardium, and does not reflect the healthy double-spiral structure. This suggests severe disruption of the tissue architecture. The maximum linear retardance value lies between 100° and 200° for most of this region, with rapid variations on a small scale, while slightly higher values of around 300° are observed closer to the outside wall. This is consistent with previous cardiac birefringence results that have shown a decrease in tissue anisotropy as healthy cardiac muscle is replaced with infarcted tissue.[12,15]

The two derived polarimetry metrics can be compared directly to DT-MRI results for the axis and degree of anisotropy. Figure 8(a) shows the

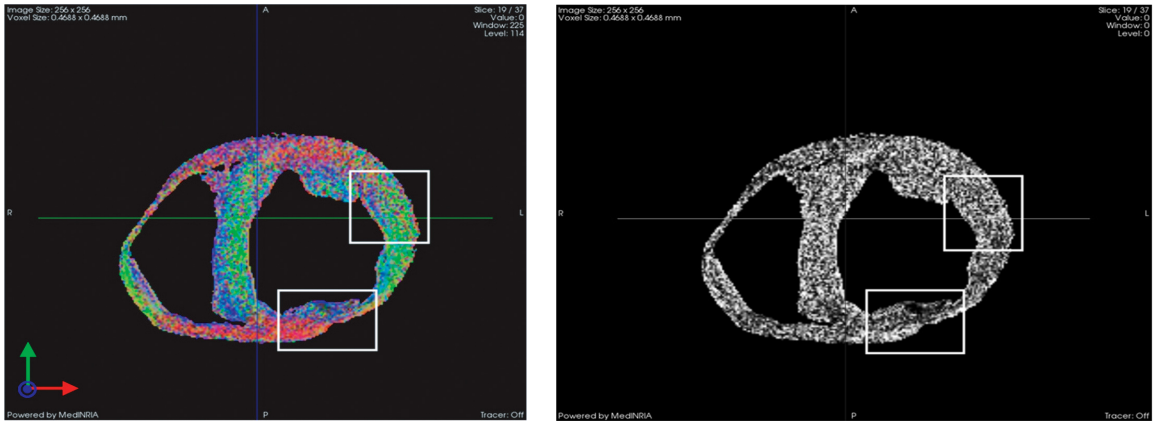

(a) (b)

Fig. 8. DTI results of anisotropy axis and magnitude. (a) Axis of anisotropy as found with DT-MRI (primary eigenvector of the diffusion tensor, corresponding to the direction of highest diffusivity). Color code: red scale corresponds to lateral component; the green scale corresponds to anterior-to-posterior component; and blue scale corresponds to superior-to-inferior component. (b) Fractional anisotropy as found with DT-MRI. (Grayscale of FA values between 0 and 1.)

diffusion tensor image, a color-coded map of the orientation of the primary eigenvector of the diffusion tensor, which is indicative of the direction of highest diffusion, with the same color-coding as Figs. 6(a) and 7(a). Once again, the orientation reflects the expected double-spiral pattern of heart muscle fibers in the healthy region (circumferential near the center of the ventricular wall, and oblique closer to the endocardium), and reveals perturbed orientation in the infarct region. Furthermore, though this is less obvious than in Fig. 7, the infarct region shows higher variations in anisotropy axis orientation than the healthy region, which is consistent with the formation of a heterogeneous scar and the disruption of the myocardial architecture. Comparison of the DT-MRI orientation image with the polarimetry images [Figs. 6(a) and 7(a)] shows that both methods yield highly consistent axis orientations for the healthy as well as the infarcted regions, with polarimetry having a higher resolution than the DT-MRI image.

Figure 8(b) shows the values of fractional anisotropy (FA), as found with DT-MRI [see Eq. (4)]: brighter regions correspond to a higher FA. The infarct region, especially near the inner wall, has a decreased FA (FA $= 0.49 \pm 0.19$, average $\pm$ standard deviation) compared to the healthy region (FA $= 0.61 \pm 0.18$), which is consistent with the findings of other groups.[20,34] Comparison with Fig. 7(b) shows that the region of decreased FA corresponds well with the region of low maximum linear retardance. The infarct region is also characterized by high spatial variation of the linear retardance value. These abrupt changes in anisotropy value were on a scale too small to be observed on the FA image. Unexpectedly, the linear retardance of the healthy region also shows a slowly increasing value of linear retardance from the outer to the inner wall. This is in contrast with the FA image, which shows a uniformly high value in the healthy regions. The tissue composition in this region is expected to be uniform, which should have yielded a uniform value of maximum linear retardance. The most likely explanation for this deviation from expected behavior is an error due to the near-parallel orientation of the probing light beam with respect to the tissue anisotropy axis: in this geometry, the apparent linear retardance will be very small [see Eq. (3)]. Under these conditions, the noise component of the apparent linear retardance can easily be larger than the real signal, leading to large errors in the reconstructed magnitude of the linear retardance, an effect which had been observed in preliminary tests of the dual projection method using a plastic material of known anisotropy axis. This explanation is supported by the fact that values of abnormally high maximum linear retardance ($\geq 600°$) almost exclusively correspond to areas in which the anisotropy axis is along the superior-to-inferior heart axis in both the healthy and the infarct sample [see Figs. 6(a) and 7(a)], corresponding to areas where the anisotropy axis would have been almost parallel to the probing beam for one or both of the sample positions.

The comparison of polarimetry and DT-MRI for assessment of myocardial tissue anisotropy shows that both methods yield similar results while having different advantages and disadvantages. Polarimetry is superior in terms of resolution, with features on the order of $\approx 300\,\mu$m being clearly distinguishable on both the anisotropy axis and the maximum linear retardance images; it also requires a relatively simple experimental apparatus. However, polarimetry has a limited depth of penetration (as some degree of polarization retention is necessary for accurate parameter extraction, limiting the distance that light can travel through depolarizing tissues) and, as used here, has no depth resolution (the signal at each pixel comes from the entire thickness of the section). Note that depth-resolved polarimetry measurements could be achieved with a polarization-sensitive optical coherence tomography (PS-OCT) system; the depth-resolution would then circumvent the problem of averaging together optical effects of different tissue layers of potentially different birefringence and orientation. Finally, polarimetry could in principle be used *in vivo*, for example using a fiber-based PS-OCT system, though many challenges (for instance, those related to limited light penetration and to cardiac wall motion) remain to be addressed.[35]

Diffusion tensor MRI, on the other hand, has the significant advantage of allowing visualization of the whole heart architecture. Furthermore, DT-MRI can be used non-invasively: while the imaging in this study was done *ex vivo*, DT-MRI can also be performed *in vivo*,[19] albeit with much lower resolutions. The very high resolutions that can be achieved with *ex vivo* imaging require very long scan times (10 hours), while the length of *in vivo* scan times is limited due to the duration of a breath-hold, and to the necessity to gate for cardiac motion.

Despite differences in technique and interrogation volume, polarimetry and diffusion tensor MRI show very good agreement for the axis of anisotropy. The magnitude results also show good concordance in most healthy and infarcted regions, except in areas where the anisotropy axis was almost parallel to the probing beam during polarimetry imaging. In these areas, the values of maximum linear retardance are overestimated, highlighting a weakness of the dual projection reconstruction in cases when the optical axis of the tissue is nearly aligned with the probing light beam. Knowledge of this limitation, however, means that it can be accounted for by rejecting the reconstructed values of maximum linear retardance for pixels whose anisotropy axis orientation is too near the probing beam orientation. Alternatively, it may be possible to improve the accuracy of the reconstruction algorithm by relying on the empirically measured behavior of the apparent linear retardance (in the presence of noise) for different anisotropy axis orientations, instead of the theoretical behavior given by Eq. (3).

4. Conclusion

Comparison of polarimetry with diffusion tensor MRI has verified that reconstructed values of maximum linear retardance and anisotropy axis orientation are generally accurate reflections of tissue anisotropy and axis, and has highlighted a limitation of polarimetry in certain sample geometries. This underscores the potential of polarimetry as a useful indicator of tissue micro-structure, especially in cases where very high resolution is required. In particular, it can provide a useful complement to information derived from histology or microscopy when tissue sectioning is an option. Additionally, the fact that polarimetry is an optical, and therefore, non-destructive method, means that it can be an attractive candidate for non-invasive assessment of injury after myocardial infarct: while the samples in this study were fixed and sectioned (as transmission results through thin sections are the most straightforward to obtain and interpret), similar results could conceivably be achieved *in vivo* without damaging tissue. Further study will be required to determine how different geometry (backscatter instead of transmission) and sample preparation (non-fixed, bulk tissue) will affect linear retardance measurements in infarcted myocardium.

Acknowledgments

Support from the Natural Sciences and Engineering Research Council of Canada, the Canadian Institutes of Health Research and the Canadian Foundation for Innovation, is gratefully acknowledged.

References

1. B. Swynghedauw, "Molecular mechanisms of myocardial remodeling," *Physiol. Rev.* **79**, 215 (1999).
2. P. Helm, L. Younes, M. Beg, D. Ennis, C. Leclercq, O. Faris, E. McVeigh, D. Kass, M. Miller, R. Winslow, "Evidence of structural remodeling in the dyssynchronous failing heart," *Circ. Res.* **98**, 125 (2006).
3. J. Garot, O. Pascal, B. Diebold, G. Derumeaux, B. Gerber, J. Dubois-Rande, J. Lima, P. Gueret, "Alterations of systolic left ventricular twist after acute myocardial infarction," *Am. J. Physiol. Heart Circ. Physiol.* **282**, H357 (2002).
4. N. Ghosh, M. Wood, I. Vitkin, "Mueller matrix decomposition for extraction of individual polarization parameters from complex turbid media exhibiting multiple scattering, optical activity, and linear birefringence," *J. Biomed. Opt.* **13**, 044036 (2008).
5. J. De Boer, T. Milner, M. van Gemert, J. Nelson, "Two-dimensional birefringence imaging in biological tissue by polarization-sensitive optical coherence tomography," *Opt. Lett.* **22**, 934–936 (1997).
6. B. Park, C. Saxer, S. Srinivas, J. Nelson, J. de Boer, "*In vivo* burn depth determination by high-speed fiber-based polarization sensitive optical coherence tomography," *J. Biomed. Opt.* **6**, 474 (2001).
7. Y. Yasuno, S. Makita, Y. Sutoh, M. Itoh, T. Yatagai, "Birefringence imaging of human skin by polarization-sensitive spectral interferometric optical coherence tomography," *Opt. Lett.* **27**, 1803–1805 (2002).
8. C. Wu, Y. Wang, L. Lu, C. Sun, C. Lu, M. Tsai, C. Yang, "Tissue birefringence of hypercholesterolemic rat liver measured with polarization-sensitive optical coherence tomography," *J. Biomed. Opt.* **12**, 064022 (2007).
9. J. De Boer, T. Milner, J. Nelson, "Determination of the depth-resolved Stokes parameters of light backscattered from turbid media by use of polarization-sensitive optical coherence tomography," *Opt. Lett.* **24**, 300–302 (1999).
10. S. Jiao, G. Yao, L. Wang, "Depth-resolved two-dimensional Stokes vectors of backscattered light and Mueller matrices of biological tissue measured with optical coherence tomography," *Appl. Opt.* **39**, 6318–6324 (2000).
11. A. Pravdin, D. Yakovlev, A. Spivak, V. Tuchin, "Mapping of optical properties of anisotropic

biological tissues," in *Proceedings of SPIE*, Vol. 5695, p. 303 (2005).
12. M. Wood, N. Ghosh, M. A. Wallenburg, S. Li, R. Weisel, B. Wilson, R. Li, A. Vitkin, "Polarization birefringence measurements for characterizing the myocardium, including healthy, infarcted, and stem cell treated regenerating cardiac tissues," (submitted to *J. Biomed. Opt.*) (2010).
13. B. Liu, M. Harman, S. Giattina, D. Stamper, C. Demakis, M. Chilek, S. Raby, M. Brezinski, "Characterizing of tissue microstructure with single-detector polarization-sensitive optical coherence tomography," *Appl. Opt.* **45**, 4464–4479 (2006).
14. B. Saleh, M. Teich, *Fundamentals of Photonics, Chapter 6.* Wiley-Interscience (1991).
15. N. Ghosh, M. Wood, S. Li, R. Weisel, B. Wilson, R. Li, I. Vitkin, "Mueller matrix decomposition for polarized light assessment of complex turbid media such as biological tissues," *J. Biophotonics* **2**(3), 145–156 (2009).
16. P. Farahmand, T. Lai, R. Weisel, S. Fazel, T. Yau, P. Menasche, R. Li, "Skeletal myoblasts preserve remote matrix architecture and global function when implanted early or late after coronary ligation into infarcted or remote myocardium," *Circulation* **118**, S130 (2008).
17. D. Le Bihan, P. van Zijl, "From the diffusion coefficient to the diffusion tensor," *NMR in Biomed.* **15**, 431–434 (2002).
18. A. Holmes, D. Scollan, R. Winslow, "Direct histological validation of diffusion tensor MRI in formaldehyde-fixed myocardium," *Magn. Reson. Med.* **44**, 157–161 (2000).
19. M. Wu, W. Tseng, M. Su, C. Liu, K. Chiou, V. Wedeen, T. Reese, C. Yang, "Diffusion tensor magnetic resonance imaging mapping the fiber architecture remodeling in human myocardium after infarction: Correlation with viability and wall motion," *Circulation* **114**, 1036 (2006).
20. E. Wu, Y. Wu, H. Tang, J. Wang, J. Yang, M. Ng, E. Yang, C. Chan, S. Zhu, C. Lau *et al.*, "Study of myocardial fiber pathway using magnetic resonance diffusion tensor imaging," *Magn. Reson. Imaging* **25**, 1048–1057 (2007).
21. G. Clarke, S. Eidt, L. Sun, G. Mawdsley, J. Zubovits, M. Yaffe, "Whole-specimen histopathology: A method to produce whole-mount breast serial sections for 3-d digital histopathology imaging," *Histopathology* **50**, 232–242 (2007).
22. P. Helm, H. Tseng, L. Younes, E. McVeigh, R. Winslow, "*Ex vivo* 3d diffusion tensor imaging and quantification of cardiac laminar structure," *Magn. Reson. Med.* **54**, 850 (2005).
23. D. LeBihan, J. Mangin, C. Poupon, C. Clark, S. Pappata, N. Molko, H. Chabriat, "Diffusion tensor imaging: Concepts and applications," *J. Magn. Reson. Imaging* **13**, 534–546 (2001).
24. P. Fillard, N. Toussaint, X. Pennec, "Medinria: DT-MRI processing and visualization software," in *Similar Tensor Workshop*, Vol. 5, p. 7 (2006).
25. H. Jiang, P. van Zijl, J. Kim, G. Pearlson, S. Mori, "Dtistudio: Resource program for diffusion tensor computation and fiber bundle tracking," *Computer Methods and Programs in Biomedicine* **81**, 106–116 (2006).
26. E. Hecht, *Optics*. Addison-Wesley (2001).
27. S. Lu, R. Chipman, "Interpretation of Mueller matrices based on polar decomposition," *J. Opt. Soc. Am. A* **13**, 1106–1113 (1996).
28. M. Wood, X. Guo, I. Vitkin, "Polarized light propagation in multiple scattering media exhibiting both linear birefringence and optical activity: Monte Carlo model and experimental methodology," *J. Biomed. Opt.* **12**, 014029 (2007).
29. N. Ghosh, M. Wood, I. Vitkin, "Influence of the order of the constituent basis matrices on the Mueller matrix decomposition-derived polarization parameters in complex turbid media such as biological tissues," *Opt. Commun.* **283**, 1200–1208 (2009).
30. X. Guo, M. Wood, A. Vitkin, "Monte Carlo study of pathlength distribution of polarized light in turbid media," *Opt. Express* **15**, 1348–1360 (2007).
31. X. Guo, M. Wood, A. Vitkin, "A Monte Carlo study of penetration depth and sampling volume of polarized light in turbid media," *Opt. Commun.* **281**, 380–387 (2008).
32. K. Schöenenberger, B. Colston, D. Maitland, L. Da Silva, M. Everett, "Mapping of birefringence and thermal damage in tissue by use of polarization-sensitive optical coherence tomography," *Appl. Opt.* **37**, 6026–6035 (1998).
33. P. Sengupta, V. Krishnamoorthy, J. Korinek, J. Narula, M. Vannan, S. Lester, J. Tajik, J. Seward, B. Khandheria, M. Belohlavek, "Left ventricular form and function revisited: Applied translational science to cardiovascular ultrasound imaging," *J. Am. Soc. Echocardiography* **20**, 539–551 (2007).
34. Y. Wu, C. Chan, J. Nicholls, S. Liao, H. Tse, E. Wu, "MR study of the effect of infarct size and location on left ventricular functional and microstructural alterations in porcine models," *J. Magn. Reson. Imaging* **29**, 305–312 (2009).
35. B. Wilson, I. Vitkin, D. Matthews, R. Oncology, "The potential of biophotonic techniques in stem cell tracking and monitoring of tissue regeneration applied to cardiac stem cell therapy," *J. Biophotonics* **2**, 669–681 (2009).